American Mineralogist, Volume 87, pages 909–921, 2002

The substitution Fe^{3+}-Al and the isosymmetric displacive phase transition in synthetic zoisite: A powder X-ray and infrared spectroscopy study

AXEL LIEBSCHER,[1, 2,*] MATTHIAS GOTTSCHALK,[1] AND GERHARD FRANZ[2]

[1]GeoForschungsZentrum Potsdam, 14473 Potsdam, Germany
[2]Technische Universität Berlin, Fachgebiet Petrologie, EB 15, 10623 Berlin, Germany

ABSTRACT

The Fe^{3+}-Al substitution in synthetic zoisite was studied in the system CFASH at 2.0 GPa and 750 °C (compositional range: 0.0–0.14 X_{ps}). The samples were characterized by powder X-ray diffraction, FTIR, and electron microprobe. Discontinuities in refined lattice parameters at ~0.05 X_{ps} are attributed to two distinct and hitherto unknown modifications, zoisite I (<0.05 X_{ps}) and zoisite II (>0.05 X_{ps}). The following lattice parameters were derived:

(zoisite I)	(zoisite II)
a (Å) = $-3.72 \times 10^{-2} \times X_{ps} + 16.1913$	a (Å) = $-8.26 \times 10^{-2} \times X_{ps} + 16.2061$
b (Å) = $6.43 \times 10^{-2} \times X_{ps} + 5.5488$	b (Å) = $8.14 \times 10^{-2} \times X_{ps} + 5.5486$
c (Å) = $3.43 \times 10^{-2} \times X_{ps} + 10.0320$	c (Å) = $1.18 \times 10^{-1} \times X_{ps} + 10.0263$
V (Å^3) = $11.4 \times X_{ps} + 901.3$	V (Å^3) = $19.3 \times X_{ps} + 901.6$

In both modifications, substitution of Fe^{3+} expands the M3 octahedron, resulting in opposed rotations of the corner-linked T1 and T2 tetrahedra of the Si_2O_7 group. The extent of rotation is limited and controls the maximum Fe^{3+} content in zoisite I and II. With increasing Fe^{3+} content, zoisite I transforms to zoisite II and zoisite II to clinozoisite. The transformation from zoisite I to II can be classified as a substitutionally induced isosymmetric displacive phase transition.

Four significant IR bands were observed at ~3250, ~3195, ~3155, and ~2170 cm^{-1}. The first three bands are attributed to the configurations $Al_2^{[M1,2]}$-O10-H···O2-$Al_2^{[M1,2]}$(Al,Fe^{3+})$^{[M3]}$, $Al_2^{[M1,2]}$-O10-H···O4-$Al_2^{[M1,2]}Fe^{3+[M3]}$, and $Al_2^{[M1,2]}$-O10-H···O4-$Al_2^{[M1,2]}Al^{[M3]}$. O10-H···O2 is bifurcated between the two symmetrically arranged O2 and O2' atoms. The band at ~2170 cm^{-1} is interpreted as the first overtone of the bending vibration of O10-H···O2. In analogy with the results from powder XRD the IR bands show discontinuities at ~0.05 X_{ps}, confirming the two modifications of zoisite.

INTRODUCTION

Systematic changes in the structures of minerals, such as changes in bond lengths and bond angles, which determine the degree of distortion of coordination polyhedra, are common in solid solutions. These changes may significantly influence the ability of a structure to incorporate trace elements, which can accompany the substitution in major elements. A detailed knowledge of how a structure reacts to an isomorphous substitution is necessary to explain for example its geochemical behavior as a host for trace elements. Furthermore, the substitution of cations of different size might induce phase transformations and can mimic structural changes in solid solutions induced by pressure or temperature (e.g., Heaney 2000).

Zoisite, the orthorhombic variety of the epidote mineral group with the idealized formula $Ca_2Al_2Al[SiO_4/Si_2O_7(O/OH)]$ contains up to 20 mol% of the hypothetical end-member $Ca_2Al_2Fe^{3+}[SiO_4/Si_2O_7(O/OH)]$ (pistacite) and its composition can be expressed as $X_{ps} = Fe^{3+}/(Fe^{3+} + Al–2)$. It can be a modally important rock-forming mineral in metabasites and metamarls, especially at high pressure in the blueschist, epidote-amphibolite, and eclogite facies. Because of its stability at high pressure, it is considered to be an important carrier of H_2O to depth in subduction zones (Schmidt and Poli 1994; Poli and Schmidt 1998) and might control the budget of Sr, Pb, Mn, Cr, and LREE in high-pressure and ultra-high-pressure metabasites (Nagasaki and Enami 1998; Brunsmann et al. 2000). Despite its petrological importance, little is known about Fe^{3+}-zoisite and the response of its structure to increasing iron content. It is not clear how the maximum amount of Fe^{3+} in zoisite is controlled by the structure and how this relates to the lattice parameters. Nothing is known about possible modifications of zoisite and the ideal or non-ideal behavior of its solid solution.

The structure of zoisite (Fig. 1) was determined by Fesenko et al. (1955, 1956), and was later refined by Dollase (1968). It contains one type of endless octahedral chain parallel to **b** with two distinct octahedral sites M1,2 and M3, which are occupied

* E-mail: alieb@gfz-potsdam.de

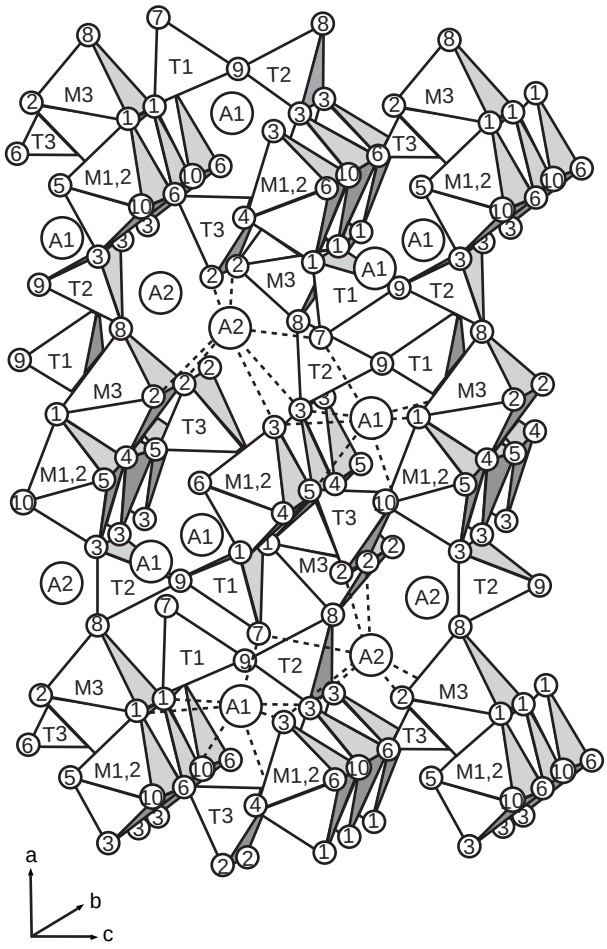

FIGURE 1. Polyhedral drawing of the zoisite structure. Octahedral chains running parallel **b** with two distinct octahedral sites M1,2 and M3 are linked by single SiO_4 tetrahedra (T3) and Si_2O_7 groups (T1 and T2). A1 and A2 are irregularly shaped, sevenfold-coordinated cavities. For clarity, bonds are shown only for selected A1 and A2 sites. O atom positions are labeled according to Dollase (1968). As discussed in the text, the Fe^{3+}-Al substitution significantly distorts the M3 octahedron and the Si_2O_7 group, resulting in significant shifts of O1, O7, and O8.

by Al (M1,2) and Al or Fe^{3+} (M3), respectively (Ghose and Tsang 1971). The octahedral chains are linked by SiO_4 tetrahedra (T3) and Si_2O_7 groups (T1 and T2) in the **a** and **c** directions. In this framework of interconnected octahedral chains there are irregularly shaped, sevenfold-coordinated cavities (A1 and A2) occupied by Ca.

In this paper we present the first systematic study of synthetic iron-free and iron-bearing zoisite using X-ray powder diffraction (XRD) and infrared spectroscopy (FTIR). We will (1) show that in the CFASH system two zoisite modifications exist; (2) show how the maximum iron content is structurally controlled in both modifications; and (3) give an explanation for a zoisite IR-band at ~2170 cm^{-1}, based on an additional hydrogen bridge in the zoisite structure.

EXPERIMENTAL AND ANALYTICAL METHODS

Sample preparation

The starting material for each experiment was an oxide-hydroxide mixture of SiO_2 (Chempur Nr. 006965, 99.99%), Al_2O_3 (Aldrich Nr. 1344-28-1, 99.99%), Fe_2O_3 (Merck, pa), and $Ca(OH)_2$ (Merck Nr. 2111, pa) weighed in stoichiometric amounts of the desired zoisite composition, with Al/Fe^{3+} ratios corresponding to zoisite compositions of 0.0, 0.04, 0.08, 0.12, and 0.16 X_{ps}. To account for the incongruent solubility of zoisite at experimental conditions and to assure quartz saturation, 10 wt% excess SiO_2 was added to each run. A 1 molar $CaBr_2$ aqueous solution was used to overcome kinetic problems, following Gottschalk (1994) and Zimmermann et al. (1996). The oxygen fugacity was controlled by the hematite-magnetite buffer, using the conventional double-capsule technique. All five capsules for the different compositions were placed in one common buffer container.

The experiments were performed at 750 °C and 2.0 GPa for 5 days, using a standard piston-cylinder apparatus with an NaCl assembly and a graphite furnace. The temperature was recorded with an accuracy of ±20 °C using a NiCrNi thermocouple placed close to the bottom of the buffer-capsule. Pressure was controlled within ±50 MPa. Quenching time (after switching off the furnace current) to <200 °C was less than 30 s.

The solid synthesis products were examined by optical microscopy, scanning electron microscopy (SEM), electron microprobe (EMP), powder X-ray diffraction with Rietveld analysis (XRD), and Fourier-transform infrared spectroscopy (FTIR).

Electron microprobe analysis

Electron microprobe (EMP) analyses of zoisite crystals were obtained from polished samples at the GeoForschungsZentrum Potsdam with a Cameca SX 50 microprobe using wavelength dispersive spectrometry (WDS) and the PAP correction program (Pouchou and Pichoir 1984). Operating conditions were 15 kV and 15 nA. Counting time for the peaks was 20 s and the background was measured for 10 s at each side of the peak. Well-characterized natural wollastonite served as the standard for Si and Ca, and Al_2O_3 and Fe_2O_3 served as standards for Al and Fe, respectively. Estimated errors are <2% rel for Si, Al, and Ca and <5% rel for Fe.

X-ray powder diffraction

The experimental products were ground by hand in an agate mortar for several minutes, diluted with Elmer's White glue and evenly spread on a circular foil. To minimize preferential orientation the powder was stirred during drying. Finally, the foil was placed into the transmission sample holder and covered with a second empty foil. Powder XRD patterns were recorded in transmission mode using a fully automated STOE STADI P diffractometer (Cu$K\alpha_1$ radiation) equipped with a primary monochromator and a position sensitive detector (PSD) with a width of 7°. The normal-focus Cu X-ray tube was operated at 40 kV and 40 mA, using a take-off angle of 6°. Intensities were recorded in the range of 2θ of 8 to 125° with a detector step size of 0.1° and a resolution of 0.02°. Counting times were selected to yield a maximum intensity of ~5000 counts. Unit-

cell parameters and other structural parameters were refined using the GSAS software package (Larson and Von Dreele 1987). The peaks were defined as pseudo-Voight with variable Lorentzian character. The peak full-width at half-maximum height (FWHM) was varied as a function of 2θ using the parameters "*U*," "*V*," "*W*" of Caglioti et al. (1958). For the Lorentzian character the parameters "*X*" and "*Y*" were used. The recorded reflections were highly symmetric due to the geometry of the STADIP diffractometer, therefore no parameters describing the asymmetry of the peaks were used. The background was fitted with a real space correlation function, which is capable of modeling the diffuse background from the amorphous foil and glue used for sample preparation. The zoisite lattice parameters (and also those of clinozoisite that was formed in experiments with higher Fe-content) were refined starting with the fractional atom coordinates, lattice constants, and space-groups reported by Dollase (1968). The anisotropic displacement factors for zoisite and clinozoisite were fixed at the values provided by Comodi and Zanazzi (1997). For each sample two refinements were performed, one with a statistically disordered distribution of Al and Fe^{3+} between the M1,2 and M3 sites in zoisite, and the other one with an ordered distribution of Al and Fe^{3+} in zoisite with Al at M1,2 and M3, and Fe^{3+} exclusively at M3 as suggested by Ghose and Tsang (1971). The Al and Fe^{3+} contents at M1,2 and M3 in zoisite were calculated according to the EMP analyses. The refinements were performed in the following sequence: scale factor, background, zero-point correction, phase fractions, Caglioti "*W*," lattice parameters, preferred orientation, atomic positions (except for hydrogen), Caglioti "*U*" and "*V*," Lorentz "*X*" and "*Y*".

Fourier-transform infrared analysis

Samples were prepared by grinding 1 mg of the product dispersed into 450 mg of KBr. The homogenized mixture was subsequently pressed under vacuum to transparent pellets, 13 mm in diameter, and dried at 110 °C for at least three days. The absorption measurements were carried out in the spectral range 3600–2000 cm^{-1} with a resolution of 0.25 cm^{-1}. All samples were measured at 25 °C, and the most iron-rich one was also measured at –180 °C, –80 °C, and 125 °C. The spectra were recorded with a Bruker IFS 66v FTIR spectrometer equipped with a globar light source, a KBr-beam splitter and a DTGS-detector, and were averaged over 256 scans. The phase correction mode of the interferogram was performed with a procedure after Merz (1965) (cf. Griffiths and de Haseth 1986) and the Norton-Beer weak mode was chosen as the apodization function. The sample chamber of the Bruker IFS 66v was evacuated to 200 Pa, therefore the influence of H_2O vapor and CO_2 was negligible. The spectra were displayed with absorbance as a function of wavenumber. After background correction, the band center, full width at half maximum (FWHM), and integral intensity were determined with the PeakFit program from Jandel Scientific.

RESULTS

Description of experimental products

Quantitative determination of the proportions of the product phases (Table 1) by Rietveld analysis yielded only zoisite and quartz for experiments Zo 3 and Zo 1, but zoisite, clinozoisite, and quartz for experiments Zo 2, Zo 4, and Zo 5. All synthesis products exhibited quartz saturation, with 2 to 6 vol% quartz. The zoisite contents decreased from 98 vol% (bulk: 0.0 X_{ps}; Zo 3) to 38 vol% (bulk: 0.16 X_{ps}; Zo 5) whereas clinozoisite contents increased from 0.5 vol% (bulk: 0.08 X_{ps}; Zo 2) to 56 vol% (bulk: 0.16 X_{ps}; Zo 5). Figure 2 shows typical SEM images of the experimental products. Crystals are idiomorphic to hypidiomorphic and generally 0.5 to 5 μm in size, but some are over 10 μm, and could easily be analyzed by EMP. Large crystals show an orthorhombic morphology with the faces

TABLE 1. Data collection, structure refinement details, lattice parameters and cell volumes for the synthetic zoisite and clinozoisite samples

Sample	Zo 3	Zo 1		Zo 2		Zo 4		Zo 5	
Zoisite (X_{ps})	0.0	0.035 (12)		0.062 (23)		0.096 (23)		0.116 (19)	
Fe^{3+}/Al distribution in zoisite	/	ordered	disordered	ordered	disordered	ordered	disordered	ordered	disordered
2θ scan range (°)	8–125	8–125		8–125		8–125		8–125	
Step interval (°)	0.02	0.02		0.02		0.02		0.02	
Observations	5848	5848		5848		5848		5848	
Parameters	73	73		78		117		120	
χ^2*	1.17	1.33	1.35	1.24	1.27	1.48	1.51	1.40	1.42
d statistics	1.63	1.44	1.42	1.54	1.51	1.38	1.35	1.32	1.30
Phases (vol%)									
zoisite	98	95	95	97	96.7	70	70	39	38
quartz	2	5	5	2.5	2.6	3	3	6	6
clinozoisite	/	/	/	0.5	0.7	27	27	55	56
zoisite									
a (Å)	16.1913 (4)	16.1900 (6)	16.1900 (6)	16.2009 (5)	16.2009 (5)	16.1983 (8)	16.1983 (8)	16.1964 (11)	16.1964 (11)
b (Å)	5.5488 (1)	5.5511 (2)	5.5511 (2)	5.5536 (2)	5.5536 (2)	5.5564 (2)	5.5564 (2)	5.5580 (3)	5.5581 (3)
c (Å)	10.0320 (3)	10.0332 (3)	10.0332 (3)	10.0336 (3)	10.0336 (3)	10.0376 (5)	10.0375 (5)	10.0400 (6)	10.0399 (6)
V (Å³)	901.30 (5)	901.70 (7)	901.70 (7)	902.76 (6)	902.76 (6)	903.43 (10)	903.42 (10)	903.8 (11)	903.79 (10)
clinozoisite									
a (Å)	/	/	/	8.8697 (13)	8.8661 (7)	8.8671 (5)	8.8672 (5)		
b (Å)	/	/	/	5.5852 (6)	5.5890 (3)	5.5886 (3)	5.5886 (3)		
c (Å)	/	/	/	10.1339 (11)	10.1370 (8)	10.1374 (6)	10.1373 (6)		
β (°)	/	/	/	115.41 (1)	115.44 (1)	115.43 (1)	115.43 (1)		
V (Å³)	/	/	/	453.46 (7)	453.61 (6)	453.67 (5)	453.68 (5)		

Note: X_{ps} = Fe^{3+} / (Fe^{3+} + Al – 2); ordered = Fe^{3+} exclusively on M3; disordered = Fe^{3+} and Al statistically distributed between M3 and M1,2; errors in parantheses represent 2σ.

* $(y_i^{observed} - y_i^{calculated})^2$ / (N – P) (y = intensity; w = 1 / y = weighting factor).

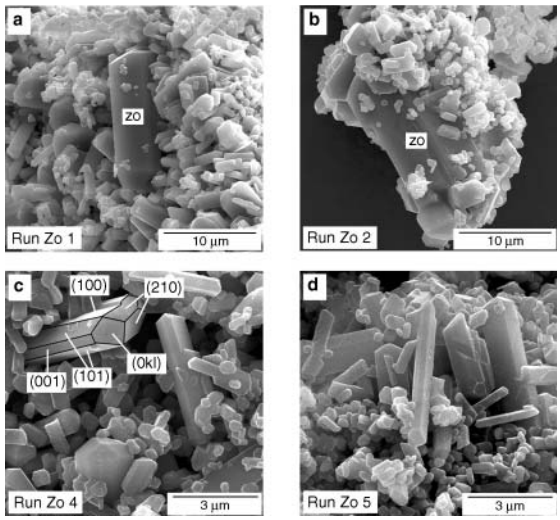

FIGURE 2. (A–D) SEM images of synthesis products (Zo 1 = 0.035 X_{ps}; Zo 2 = 0.062 X_{ps}; Zo 4 = 0.096 X_{ps}; Zo 5 = 0.116 X_{ps}). Zoisite crystals up to 20 µm in length are seen in a matrix of crystals with lengths <5 µm. Typically, (100), (001), (101), (210), and (0*kl*) faces are developed.

(100), (001), (101), (210), and (0*kl*) that are typically developed in zoisite (Fig. 2c; indexing made by comparison with a crystal drawing in Tröger 1982). Within the individual experimental products the zoisite crystals are homogeneous (Table 2). Various analyses on single grains were made wherever the grains were large enough and no zoning was observed. In the iron-bearing experiments zoisite was generally poorer in iron than the corresponding bulk composition (Table 2). This is especially true for experiments Zo 4 and Zo 5 in which clinozoisite was an important additional product phase.

X-ray diffraction

The lattice parameters and atom coordinates of all of the samples were easily and precisely refined with the Rietveld method. χ^2 ranged from 1.17 to 1.51 and the Durbin-Watson factor from 1.63 to 1.30 (Table 1). The differences between the refinements assuming an ordered and statistic distribution of iron were minor, but in view of their better statistics (Table 1), only the former will be referred to in the following.

Lattice parameters and atom coordinates. Lattice parameters of zoisite (Table 1, Fig. 3) show more or less pronounced discontinuities (positive offsets for *a*, *b*, and *V*, negative offset for *c*) at compositions between 0.035 and 0.062 X_{ps}, pointing to an iron-poor zoisite I and an iron-rich zoisite II. In both modifications *a* correlates negatively, whereas *b*, *c*, and *V* correlate positively with increasing iron content. Regression lines yield

$$a^{zo\ I}\ (Å) = -3.72 \times 10^{-2} \times X_{ps} + 16.1913$$
$$a^{zo\ II}\ (Å) = -8.26 \times 10^{-2} \times X_{ps} + 16.2061$$
$$b^{zo\ I}\ (Å) = 6.43 \times 10^{-2} \times X_{ps} + 5.5488$$
$$b^{zo\ II}\ (Å) = 8.14 \times 10^{-2} \times X_{ps} + 5.5486$$
$$c^{zo\ I}\ (Å) = 3.43 \times 10^{-2} \times X_{ps} + 10.0320$$
$$c^{zo\ II}\ (Å) = 1.18 \times 10^{-1} \times X_{ps} + 10.0263$$
$$V^{zo\ I}\ (Å^3) = 11.4 \times X_{ps} + 901.3$$
$$V^{zo\ II}\ (Å^3) = 19.3 \times X_{ps} + 901.6.$$

TABLE 2. Average electron microprobe analyses of synthetic zoisites

Sample	Zo 3	Zo 1	Zo 2	Zo 4	Zo 5
Bulk (X_{PS})	0.0	0.04	0.08	0.12	0.16
*N**	14	25	22	23	35
SiO_2	39.86 (54)	39.63 (66)	39.93 (50)	39.25 (91)	39.37 (66)
Al_2O_3	33.38 (65)	32.92 (82)	32.72 (63)	32.04 (75)	31.88 (68)
Fe_2O_3	0.04 (4)	0.60 (16)	1.04 (39)	1.68 (34)	2.02 (25)
CaO	24.69 (34)	24.31 (49	24.61 (43)	24.16 (48)	24.22 (39)
Total	97.97 (1.32)	97.46 (1.66)	98.30 (1.17)	97.13 (1.77)	97.49 (1.42)
Formula recalculation based on 12.5 O atoms per formula unit					
SI	3.02 (2)	3.02 (2)	3.02 (2)	3.01 (2)	3.02 (2)
AL	2.98 (3)	2.96 (4)	2.92 (4)	2.90 (4)	2.88 (3)
Fe^{3+}	0.00 (0)	0.04 (1)	0.06 (2)	0.10 (2)	0.12 (2)
Total	2.98 (3)	3.00 (4)	2.98 (3)	3.00 (3)	3.00 (3)
CAO	2.00 (2)	1.99 (2)	2.00 (2)	1.99 (2)	1.99 (2)
X_{ps}	0.0 (0)	0.035 (12)	0.062 (23)	0.096 (23)	0.116 (19)

Note: $X_{ps} = Fe^{3+} / (Fe^{3+} + Al - 2)$; errors in parantheses represent 2σ .
* N = number of individual grains analyzed.

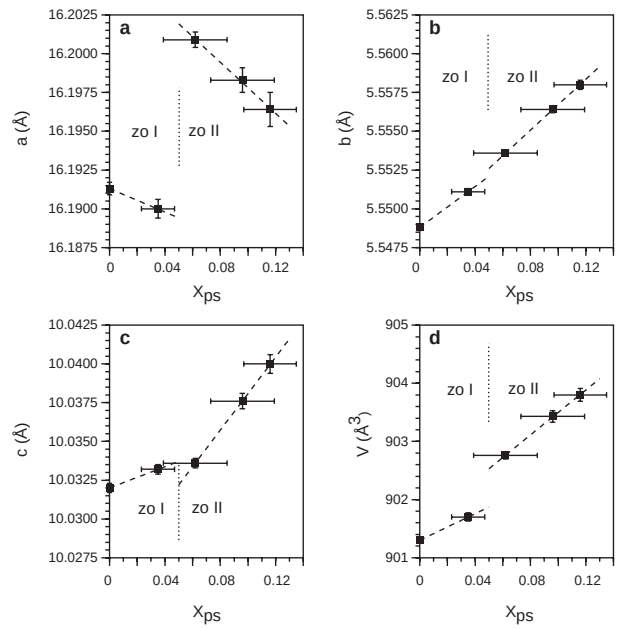

FIGURE 3. Variation of lattice constants and cell volume of zoisite with iron content. Discontinuities at ~0.05 X_{ps} with a positive offset in *a*, *b*, and *V* and a negative offset in *c* point to the two modifications zoisite I and zoisite II.

The lattice parameters of zoisite II exhibit a stronger dependence on iron content than those of zoisite I. The refined fractional atom coordinates are, within error, generally independent of iron content (Table 3). Exceptions are O1, O7, and O8 (Table 3, Fig. 4), the coordinates of which shift significantly with increasing iron content and, like the lattice parameters, show discontinuities between zoisite I and II (Fig. 4).

A polyhedra. The A1 and A2 polyhedra remain relatively rigid with increasing iron content. Using a cut-off value of 2.90 Å (Dollase 1968), the A1 and A2 cations are sevenfold-coordinated (Table 4). The mean A1-O distances are generally shorter than the mean A2-O distances and both show practically no variations with iron content (Table 4). The displacements of O1, O7, and O8 (Table 3) are mirrored by decreasing A1-O1

TABLE 3. Fractional atom coordinates in synthetic zoisites

Sample		Zo 3	Zo 1	Zo 2	Zo 4	Zo 5
Zoisite [X_{ps}]		0.0 (0)	0.035 (12)	0.062 (23)	0.096 (23)	0.116 (19)
A1	*x*	0.3666 (4)	0.3671 (5)	0.3671 (5)	0.3668 (7)	0.3652 (13)
	y	0.25	0.25	0.25	0.25	0.25
	z	0.4376 (6)	0.4380 (9)	0.4375 (8)	0.4361 (12)	0.4376 (19)
A2	*x*	0.4521 (4)	0.4515 (5)	0.4517 (4)	0.4518 (7)	0.4531 (12)
	y	0.25	0.25	0.25	0.25	0.25
	z	0.1130 (6)	0.1123 (8)	0.1131 (7)	0.1113 (10)	0.1120 (17)
M1,2	*x*	0.2498 (5)	0.2509 (7)	0.2500 (6)	0.2510 (9)	0.2516 (16)
	y	0.9972 (11)	0.9957 (14)	0.9966 (14)	0.995 (2)	0.993 (3)
	z	0.1905 (5)	0.1899 (7)	0.1902 (7)	0.1904 (10)	0.1887 (16)
M3	*x*	0.1057 (6)	0.1039 (8)	0.1051 (7)	0.1058 (10)	0.1059 (17)
	y	0.75	0.75	0.75	0.75	0.75
	z	0.3013 (8)	0.3015 (10)	0.3011 (9)	0.3027 (13)	0.303 (2)
T1	*x*	0.0817 (5)	0.0817 (7)	0.0813 (6)	0.0834 (10)	0.0842 (17)
	y	0.25	0.25	0.25	0.25	0.25
	z	0.1054 (8)	0.1038 (11)	0.1052 (10)	0.1000 (15)	0.100 (2)
T2	*x*	0.4101 (5)	0.4106 (7)	0.4105 (6)	0.4121 (10)	0.4139 (17)
	y	0.75	0.75	0.75	0.75	0.75
	z	0.2816 (8)	0.2841 (12)	0.2830 (11)	0.2819 (16)	0.2875 (3)
T3	*x*	0.1605 (5)	0.1610 (7)	0.1603 (6)	0.1615 (9)	0.1596 (15)
	y	0.25	0.25	0.25	0.25	0.25
	z	0.4349 (9)	0.4358 (13)	0.4365 (12)	0.4385 (18)	0.434 (3)
O1	*x*	0.1303 (7)	0.1323 (9)	0.1303 (8)	0.1334 (13)	0.136 (2)
	y	–0.004 (2)	–0.006 (3)	–0.006 (3)	–0.017 (4)	–0.030 (6)
	z	0.1434 (10)	0.1424 (14)	0.1430 (13)	0.1442 (19)	0.143 (3)
O2	*x*	0.1018 (6)	0.1034 (9)	0.1024 (8)	0.1028 (12)	0.1047 (20)
	y	0.0112 (19)	0.012 (3)	0.009 (2)	0.007 (3)	0.004 (6)
	z	0.4288 (11)	0.4294 (15)	0.4308 (14)	0.433 (2)	0.429 (3)
O3	*x*	0.3601 (7)	0.3601 (10)	0.3598 (8)	0.3587 (13)	0.359 (2)
	y	0.992 (2)	0.996 (4)	0.994 (3)	0.995 (5)	0.993 (8)
	z	0.2439 (11)	0.2443 (14)	0.2442 (13)	0.2450 (18)	0.247 (3)
O4	*x*	0.2212 (10)	0.2212 (15)	0.2203 (13)	0.221 (2)	0.224 (4)
	y	0.75	0.75	0.75	0.75	0.75
	z	0.3016 (15)	0.303 (2)	0.3028 (19)	0.305 (3)	0.305 (5)
O5	*x*	0.2265 (11)	0.2257 (15)	0.2244 (13)	0.225 (2)	0.226 (4)
	y	0.25	0.25	0.25	0.25	0.25
	z	0.3115 (15)	0.313 (2)	0.3137 (19)	0.309 (3)	0.304 (5)
O6	*x*	0.2724 (10)	0.2718 (14)	0.2712 (12)	0.2738 (19)	0.275 (3)
	y	0.75	0.75	0.75	0.75	0.75
	z	0.0600 (16)	0.062 (2)	0.062 (2)	0.061 (3)	0.060 (5)
O7	*x*	0.9892 (10)	0.9916 (15)	0.9917 (13)	0.994 (2)	0.999 (3)
	y	0.25	0.25	0.25	0.25	0.25
	z	0.1636 (16)	0.165 (2)	0.165 (2)	0.169 (3)	0.175 (5)
O8	*x*	0.9985 (12)	0.9960 (17)	0.9976 (15)	0.993 (2)	0.985 (4)
	y	0.75	0.75	0.75	0.75	0.75
	z	0.2965 (16)	0.299 (2)	0.295 (2)	0.301 (3)	0.302 (5)
O9	*x*	0.4190 (10)	0.4203 (14)	0.4204 (12)	0.4212 (19)	0.423 (3)
	y	0.75	0.75	0.75	0.75	0.75
	z	0.4425 (19)	0.439 (3)	0.438 (2)	0.435 (4)	0.434 (6)
O10	*x*	0.2676 (11)	0.2664 (15)	0.2681 (14)	0.269 (2)	0.270 (4)
	y	0.25	0.25	0.25	0.25	0.25
	z	1.0741 (14)	1.0701 (19)	1.0730 (17)	1.074 (3)	1.067 (5)
H	*x*			0.26 (not refined)		
	y			0.25 (not refined)		
	z			0.95 (not refined)		

Note: $X_{ps} = Fe^{3+} / (Fe^{3+} + Al - 2)$; errors in parantheses represent 2σ.

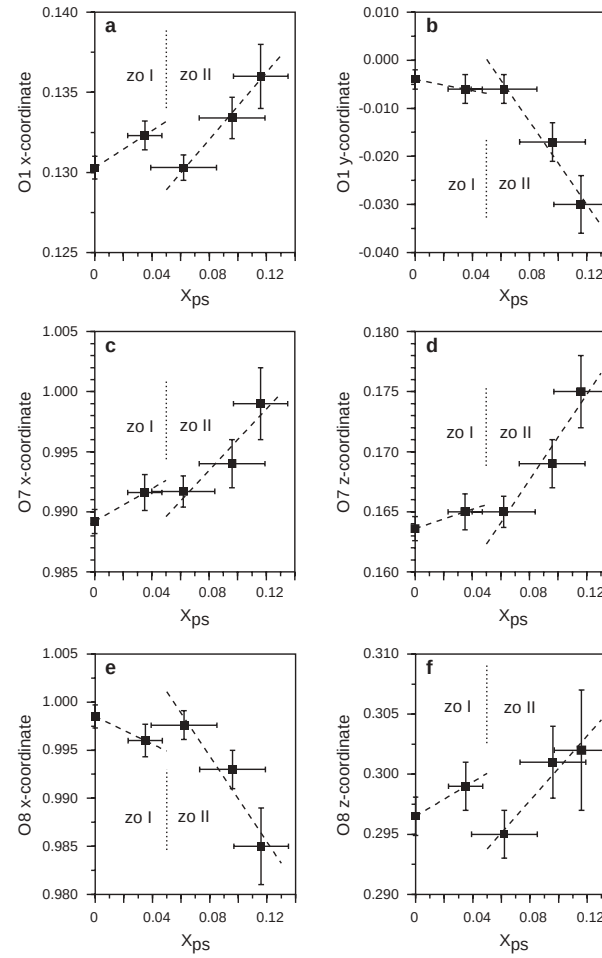

FIGURE 4. Variation of fractional atom coordinates of O1, O7, and O8 with iron content. Discontinuities between zoisite I and II occur at the same iron content as lattice constants.

and A2-O8 distances and a significant increase in the A1-O7 value (Table 4).

M1,2 octahedron. The M1,2 octahedron is relatively undistorted and shows only minor changes with increasing iron content. The mean M1,2-O distance is shorter than that of the M3 octahedron (Table 4). Only the angles O1-M1,2-O4 and O5-M1,2-O10 deviate significantly from the ideal octahedral value of 90° (Table 5). The shared edges O1-O4, O4-O6, O5-O10 are significantly shorter than the non-shared edges (Table 6). The displacement of O1 is mirrored by changes in the O1-O6 distance (Tables 3 and 6). The volume (8.8–9.0 $Å^3$) is essentially constant over the entire compositional range (Table 6).

M3 octahedron. The M3 octahedron is strongly distorted and shows significant changes with increasing iron content. The mean M3-O distances are generally longer than those of the M1,2 octahedron (Table 4) and individual M3-O distances are very inhomogeneous although they become more homogeneous with increasing iron content (Table 4). More than half of the angles deviate significantly from the ideal octahedral values of 90° and 180°, respectively (Table 5). The O1-M3-O1' and O1-M3-O2 angles in particular display a strong correlation with iron content. The individual O-O distances within the M3 octahedron are very inhomogeneous and the mean O-O distances are approximately 0.1 Å longer than in the M1,2 octahedron (Table 6). Consequently, M3 has a volume 0.7 to 1 $Å^3$ larger than M1,2 (Table 6). The O1-O1', O1-O8, and O2-O8 distances in particular vary significantly with increasing iron content, reflecting the displacements of O1 and O8 (Tables 3 and 6). The displacement of O8 is best seen in the distance between the two apical O atoms O4 and O8, which increases from 3.61 Å to 3.87 Å with a clear negative offset between the two modifications (Table 6, Fig. 5).

TABLE 4. Bond lengths (Å) in synthetic zoisites

Sample	Zo 3	Zo 1	Zo 2	Zo 4	Zo 5
Zoisite (X_{ps})	0.0 (0)	0.035 (12)	0.062 (23)	0.096 (23)	0.116 (19)
A1 polyhedron					
A1-O1 2×	2.475 (12)	2.457 (16)	2.468 (14)	2.46 (2)	2.40 (3)
A1-O3 2×	2.415 (12)	2.405 (18)	2.409 (16)	2.39 (2)	2.39 (4)
A1-O5	2.598 (16)	2.61 (2)	2.62 (2)	2.63 (3)	2.62 (6)
A1-O6	2.565 (16)	2.57 (2)	2.57 (2)	2.60 (3)	2.57 (5)
A1-O7	2.229 (18)	2.27 (2)	2.26 (2)	2.32 (3)	2.45 (6)
A1-O9 * 2×	2.902 (5)	2.906 (7)	2.908 (6)	2.915 (10)	2.933 (18)
Mean A1-O†	2.453 (14)	2.453 (18)	2.458 (17)	2.46 (2)	2.46 (4)
A2 polyhedron					
A2-O2 2x	2.505 (12)	2.504 (16)	2.486 (16)	2.45 (2)	2.50 (4)
A2-O2' 2x	2.794 (12)	2.824 (16)	2.819 (14)	2.83 (2)	2.84 (4)
A2-O3 2x	2.448 (12)	2.437 (18)	2.445 (16)	2.47 (2)	2.49 (4)
A2-O7	2.321 (16)	2.33 (2)	2.32 (2)	2.31 (3)	2.26 (5)
A2-O8 * 2x	3.015 (8)	3.004 (10)	3.018 (10)	2.990 (14)	2.96 (2)
A2-O10 *	3.013 (18)	3.03 (3)	3.00 (2)	2.98 (4)	3.01 (6)
Mean A2-O‡	2.545 (13)	2.551 (17)	2.546 (16)	2.54 (2)	2.56 (4)
M1,2 octahedron					
M1,2-O1	1.991 (12)	1.979 (16)	1.997 (14)	1.96 (2)	1.93 (3)
M1,2-O3	1.864 (12)	1.850 (16)	1.859 (14)	1.83 (2)	1.84 (3)
M1,2-O4	1.827 (12)	1.835 (14)	1.839 (14)	1.85 (2)	1.84 (3)
M1,2-O5	1.893 (12)	1.917 (16)	1.920 (14)	1.90 (2)	1.88 (4)
M1,2-O6	1.932 (12)	1.900 (16)	1.911 (14)	1.92 (2)	1.91 (4)
M1,2-O10	1.848 (10)	1.871 (14)	1.857 (12)	1.86 (2)	1.90 (3)
Mean M1,2-O	1.893 (12)	1.892 (15)	1.897 (14)	1.89 (2)	1.88 (3)
M3 octahedron					
M3-O1 2x	2.129 (12)	2.142 (16)	2.126 (16)	2.10 (2)	2.07 (4)
M3-O2 2x	1.934 (12)	1.938 (16)	1.939 (14)	1.94 (2)	1.90 (3)
M3-O4	1.871 (18)	1.90 (3)	1.87 (2)	1.87 (4)	1.92 (6)
M3-O8	1.74 (2)	1.75 (3)	1.74 (2)	1.82 (4)	1.95 (6)
Mean M3-O	1.956 (14)	1.97 (2)	1.957 (17)	1.96 (3)	1.97 (4)
T1 tetrahedron					
T1-O1 2x	1.659 (12)	1.686 (16)	1.672 (14)	1.75 (2)	1.83 (4)
T1-O7	1.607 (16)	1.58 (2)	1.57 (2)	1.60 (3)	1.57 (5)
T1-O9	1.634 (18)	1.66 (3)	1.68 (2)	1.66 (4)	1.67 (6)
Mean T1-O	1.640 (15)	1.65 (2)	1.649 (17)	1.69 (3)	1.73 (5)
T2 tetrahedron					
T2-O3 2x	1.614 (12)	1.639 (18)	1.630 (16)	1.65 (2)	1.67 (4)
T2-O8	1.63 (2)	1.61 (3)	1.61 (2)	1.56 (4)	1.47 (6)
T2-O9	1.620 (18)	1.56 (2)	1.56 (2)	1.54 (3)	1.48 (5)
Mean T2-O	1.620 (16)	1.61 (2)	1.608 (18)	1.60 (3)	1.57 (5)
T3 tetrahedron					
T3-O2 2x	1.632 (10)	1.620 (14)	1.637 (14)	1.651 (18)	1.64 (3)
T3-O5	1.635 (18)	1.62 (2)	1.61 (2)	1.65 (3)	1.70 (6)
T3-O6	1.660 (18)	1.67 (2)	1.68 (2)	1.62 (3)	1.65 (5)
Mean T3-O	1.640 (14)	1.633 (17)	1.641 (17)	1.64 (2)	1.66 (4)

Note: X_{ps} = Fe^{3+} / (Fe^{3+} + Al – 2); errors in parantheses represent 2σ.
* Not considered as bond in calculation of mean bond length (see text for explanation).
† Without A1-O9 ‡ without A2-O8 and A2-O10.

TABLE 5. Selected interatomic angles (°) in synthetic zoisites

Sample	Zo 3	Zo 1	Zo 2	Zo 4	Zo 5
Zoisite (X_{ps})	0.0 (0)	0.035 (12)	0.062 (23)	0.096 (23)	0.116 (19)
O–M–O					
Angles that deviate more than 5 ° from the ideal octahedral value					
O1-M1,2-O4	84.1 (7)	83.7 (1.0)	83.4 (8)	82.4 (1.2)	83 (2)
O4-M1,2-O5	96.6 (6)	95.5 (8)	95.4 (7)	95.6 (1.2)	97 (2)
O5-M1,2-O10	82.8 (4)	83.4 (6)	83.5 (5)	82.2 (1.0)	81.9 (1.4)
O4-M1,2-O10	174.3 (1.4)	172.4 (1.6)	173.9 (1.8)	174.0 (1.8)	175 (5)
O1-M3-O1'	79.7 (7)	78.4 (8)	79.2 (8)	76.2 (1.2)	72 (2)
O1-M3-O4 2×	79.3 (6)	77.8 (8)	79.3 (7)	78.3 (1.0)	76.9 (1.8)
O1-M3-O8 2×	99.6 (6)	101.7 (8)	99.6 (8)	101.9 (1.2)	103.6 (1.8)
O2-M3-O2'	97.1 (8)	97.1 (1.0)	95.7 (1.0)	94.9 (1.2)	96 (2)
O1-M3-O2 2×	168.1 (6)	165.3 (1.0)	167.8 (8)	166.4 (1.2)	163 (2)
O–T–O					
Angles that deviate more than 5 ° from the ideal tetrahedral value					
O1-T1-O1'	116.3 (1.0)	115.0 (1.4)	116.5 (1.2)	116.2 (1.8)	117 (3)
O1-T1-O9 2×	103.5 (5)	103.8 (7)	103.6 (6)	105.9 (8)	105.8 (1.2)
O8-T2-O9	113.5 (1.0)	115.2 (1.4)	113.2 (1.4)	117 (2)	122 (4)
O5-T3-O6	98.3 (8)	99.2 (1.2)	98.5 (1.0)	101.3 (1.6)	100 (3)
Angles within the Si_2O_7 group					
T1-O9-T2	174.5 (1.2)	173.1 (1.6)	173.2 (1.4)	172 (2)	170 (4)
O1-O9-O3 2×	102 (1)	100 (1)	101 (1)	99 (2)	97 (4)
O-O9-O8	118 (1)	121 (1)	120 (1)	123 (2)	130 (4)

Note: X_{ps} = Fe^{3+} / (Fe^{3+} + Al – 2); errors in parantheses represent 2σ.

TABLE 6. Selected O-O and cation distances (Å) and polyhedra volumes (Å³) in synthetic zoisites

Sample	Zo 3	Zo 1	Zo 2	Zo 4	Zo 5
Zoisite (X_{ps})	0.0 (0)	0.035 (12)	0.062 (23)	0.096 (23)	0.116 (19)
M1,2 octahedron					
O1-O4	2.56 (2)	2.55 (2)	2.56 (2)	2.51 (3)	2.50 (4)
O4-O6	2.56 (2)	2.55 (2)	2.55 (2)	2.60 (3)	2.60 (4)
O5-O10	2.47 (2)	2.52 (2)	2.52 (2)	2.47 (3)	2.48 (4)
O1-O6	2.80 (2)	2.75 (2)	2.79 (2)	2.75 (3)	2.69 (4)
O1-O10	2.72 (2)	2.70 (2)	2.74 (2)	2.74 (3)	2.77 (4)
O4-O5	2.78 (2)	2.78 (2)	2.78 (2)	2.78 (3)	2.79 (4)
O6-O10	2.78 (2)	2.78 (2)	2.78 (2)	2.79 (3)	2.78 (4)
Mean O-O	2.67 (2)	2.67 (2)	2.68 (2)	2.67 (3)	2.67 (4)
Volume	9.0 (2)	9.0 (2)	9.0 (2)	8.9 (3)	8.8 (4)
M3 octahedron					
O1-O4 2×	2.56 (2)	2.55 (4)	2.56 (3)	2.51 (3)	2.48 (6)
O2-O8 2×	2.58 (3)	2.62 (4)	2.61 (3)	2.63 (3)	2.71 (6)
O1-O2 2×	2.90 (2)	2.92 (2)	2.93 (2)	2.95 (3)	2.92 (5)
O1-O8 2×	2.97 (3)	3.03 (4)	2.96 (3)	3.05 (3)	3.16 (6)
O1-O1'	2.73 (2)	2.71 (2)	2.71 (2)	2.59 (3)	2.43 (5)
O2-O2'	2.90 (2)	2.91 (2)	2.88 (2)	2.86 (3)	2.82 (5)
O4-O8	3.61 (3)	3.65 (4)	3.61 (3)	3.69 (3)	3.87 (6)
Mean O-O	2.76 (2)	2.77 (2)	2.76 (2)	2.76 (3)	2.77 (5)
Volume	9.7 (2)	9.8 (2)	9.7 (2)	9.7 (3)	9.8 (5)
T1 tetrahedron					
O1-O1'	2.82 (2)	2.84 (2)	2.84 (2)	2.97 (3)	3.12 (5)
O1-O9 2×	2.57 (2)	2.63 (3)	2.63 (3)	2.72 (4)	2.79 (6)
Mean O-O	2.67 (2)	2.69 (3)	2.69 (3)	2.76 (4)	2.82 (6)
Volume	2.24 (5)	2.30 (8)	2.28 (8)	2.46 (11)	2.60 (17)
T2 tetrahedron					
O3-O8 2×	2.64 (2)	2.62 (3)	2.64 (3)	2.61 (4)	2.51 (6)
O8-O9	2.72 (2)	2.68 (3)	2.65 (3)	2.64 (4)	2.58 (6)
Mean O-O	2.65 (2)	2.63 (3)	2.63 (3)	2.61 (4)	2.56 (6)
Volume	2.17 (5)	2.14 (7)	2.12 (7)	2.09 (10)	1.97 (14)
T3 tetrahedron					
O2-O2'	2.65 (2)	2.65 (2)	2.68 (2)	2.70 (2)	2.75 (4)
Mean O-O	2.67 (2)	2.66 (3)	2.68 (3)	2.68 (4)	2.70 (6)
Volume	2.23 (5)	2.21 (7)	2.24 (8)	2.26 (10)	2.31 (15)
Si_2O_7 group					
O7-O8	4.62 (3)	4.66 (4)	4.62 (4)	4.73 (6)	4.80 (11)

Note: X_{ps} = Fe^{3+} / (Fe^{3+} + Al – 2); errors in parantheses represent 2σ.

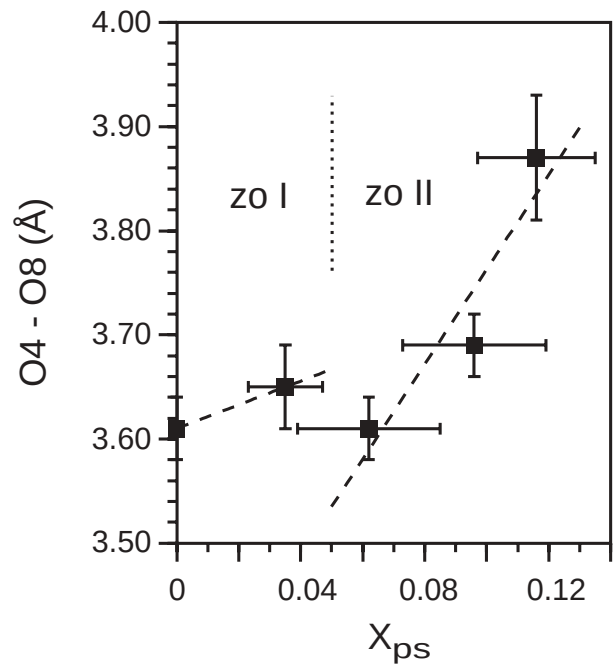

FIGURE 5. Increasing distance between the two apical O atoms O4 and O8 of the M3 octahedron of zoisite with increasing iron content. The discontinuity marks the transition between zoisite I and II.

Tetrahedra. T1 and T2 vary significantly with increasing iron content and become more distorted. The mean T1-O distances increase from 1.64 to 1.73 Å whereas the mean T2-O distances decrease from 1.62 to 1.57 Å (Table 4). The O-T-O angles in T1 and T2 can deviate up to 13° from the ideal tetrahedral value of 109° (Table 5). In T1 the mean O-O distance as well as the volume increase whereas in T2 they decrease (Table 6) with increasing iron content. In T3 only O2-O2' increases with increasing iron content; all other structural values remain approximately constant (Tables 4, 5, and 6).

The geometry of the Si_2O_7 group changes significantly with increasing iron content, due to rotation of the T1 and T2 tetrahedra. The T1-O9-T2 and O1-O9-O3 angles tighten slightly, whereas the O7-O9-O8 angle increases significantly (Table 5, Fig. 6a). Consequently, the O7-O8 distance increases (Table 6, Fig. 6b).

FTIR spectroscopy

Comparison of the measured IR spectra with published spectra of natural zoisite and clinozoisite samples (Langer and Raith 1974) allows precise assignment of the IR bands. In experiments Zo 3, Zo 1, and Zo 2 only zoisite bands were detected, whereas in Zo 4 and Zo 5 additional clinozoisite bands occur (Table 7). No bands were detected between approximately 2900 and 2250 cm^{-1} (Table 7).

In the spectral range 3600 to 2900 cm^{-1} the spectra of iron-free zoisite can be fitted with a main band at 3152.92 cm^{-1} (band 5) with satellites at 3214.8 cm^{-1} and 3065.5 cm^{-1} (bands 3 and 7) and a less pronounced band at 3259.6 cm^{-1} (band 2) (Table 7, Fig. 7). In iron-bearing zoisite an additional, relatively pronounced band is observed at ~3195 cm^{-1} (band 4), with satellites at ~3290 and ~3100 cm^{-1} (bands 1 and 6) (Table 7, Fig. 7). Due to their low intensities, bands 1 and 3 could not be resolved in all experiments (Table 7, Fig. 8a). Clinozoisite (only in Zo 4 and Zo 5) has a main band at ~3330 cm^{-1} (band 2) and a satellite at ~3405 cm^{-1} (band 1) (Table 7, Fig. 8a). The relative bulk intensities of the zoisite and clinozoisite bands in this spectral range agree well with the modal abundance of these phases as determined by XRD (Tables 1 and 8). The relative intensity of zoisite band 4 continuously increases from 0 to 16% with increasing iron content, whereas that of zoisite band 5 concomitantly decreases from 89% to 67% (Table 8). The

TABLE 7. Positions (cm^{-1}) and widths (full width at half maximum, FWHM) (cm^{-1}) of IR bands (range 3600–2000 cm^{-1} at 25 °C) in synthetic zoisites (zo) and clinozoisites (czo)

Sample	Zo 3	Zo 1	Zo 2	Zo 4	Zo 5
Zoisite (X_{ps})	0.0 (0)	0.035 (12)	0.062 (23)	0.096 (23)	0.116 (19)
Band					
Czo					
1 position	/	/	n.r.	3405.4 (4)	3410.0 (3)
FWHM				54.5 (1.1)	65.2 (8)
2 position	/	/	n.r.	3331.97 (10)	3334.99 (4)
FWHM				52.3 (2)	48.95 (9)
Zo					
1 position	/	3286.2 (1.6)	3292 (6)	3290.5 (1.8)	n.r.
FWHM		47.3 (1.7)	49 (5)	38 (3)	
2 position	3259.6 (5)	3255.6 (9)	3257 (4)	3249 (4)	3243 (5)
FWHM	59.9 (9)	49 (4)	46 (11)	56 (16)	52 (23)
3 position	3214.8 (9)	3226.3 (7)	n.r.	n.r.	n.r.
FWHM	65 (3)	37 (4)			
4 position	/	3194.6 (9)	3198 (4)	3191.4 (9)	3190.8 (1.8)
FWHM		46 (3)	46 (12)	46 (4)	53 (9)
5 position	3152.92 (3)	3154.59 (7)	3159.0 (5)	3159.4 (2)	3160.4 (4)
FWHM	52.77 (8)	53.2 (2)	55.7 (7)	57.3 (4)	56.2 (7)
6 position	/	3098.8 (4)	3097.3 (1.2)	3102.9 (6)	3102.0 (1.4)
FWHM		39.3 (1.5)	39 (4)	43 (3)	50 (7)
7 position	3065.5 (3)	3058.2 (4)	3060.9 (1.6)	3065.7 (6)	3060.4 (1.3)
FWHM	53.5 (1.1)	46.2 (9)	39 (3)	38.0 (1.3)	43 (3)
8 position	2194.0 (3)	2196.3 (9)	2197.1 (1.3)	2201.2 (1.2)	n.r.
FWHM	18.6 (5)	31.9 (1.2)	39.4 (1.8)	33 (2)	
9 position	2172.53 (3)	2171.13 (4)	2169.04 (7)	2167.35 (4)	2167.50 (5)
FWHM	24.18 (12)	26.79 (11)	27.6 (2)	30.4 (2)	31.6 (1)
10 position	2146.9 (3)	2144.06 (18)	2141.6 (3)	2140.6 (3)	2140.8 (4)
FWHM	18.5 (6)	16.6 (5)	17.4 (9)	18.0 (7)	15.2 (8)

Note: X_{ps} = Fe^{3+} / (Fe^{3+} + Al – 2); clinozoisite composition unknown (see text); / = band not present; n.r. = position of band not resolvable; errors in parantheses represent 2σ.

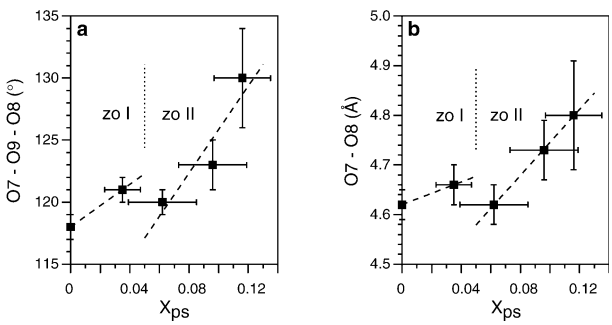

FIGURE 6. Changes in the Si_2O_7 group of zoisite with iron content. The O7-O9-O8 angle and the O7-O8 distance increase significantly with increasing iron content, which reflects rotation of T1 and T2 in response to the expansion of M3.

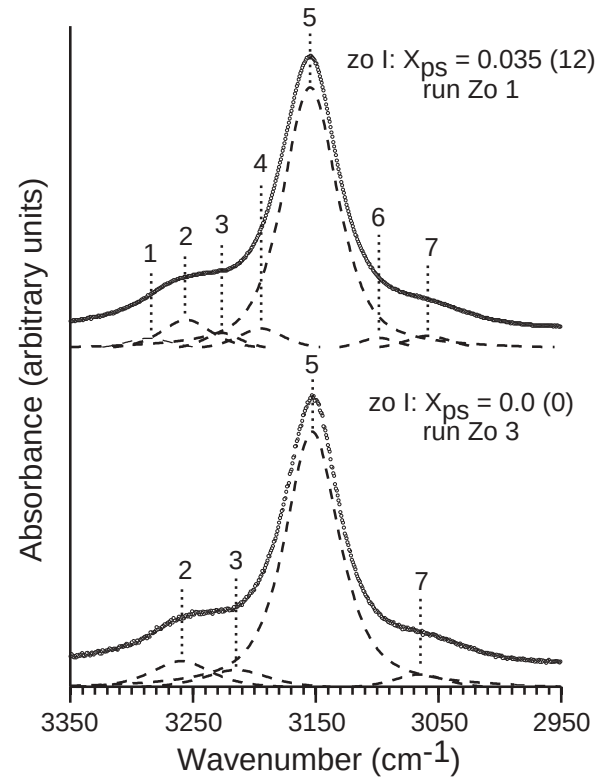

FIGURE 7. FTIR spectra of synthetic zoisite I in the spectral range 3350–2950 cm^{-1}. The spectra of iron-free zoisite (lower part) can be fitted with four bands, that of the iron-bearing zoisite (upper part) with three additional bands.

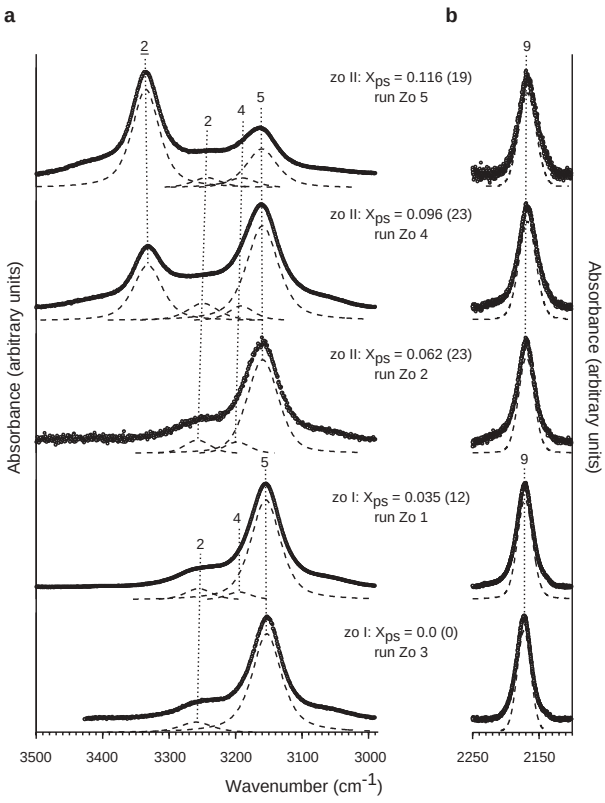

FIGURE 8. FTIR spectra and fit of significant zoisite and clinozoisite bands in the spectral ranges 3500–3000 cm^{-1} (**a**) and 2250–2100 cm^{-1} (**b**) for all samples. 2, 4, 5, and 9 are zoisite bands, and 2 is a clinozoisite band, which is found in the iron-rich samples Zo 4 and Zo 5. For clarity, clinozoisite band 1 and zoisite bands 1, 3, 6, 7, 8, and 10 (see Table 7) are not plotted due to their low intensities.

TABLE 8. Relative bulk intensities (%) of zoisite and clinozoisite IR-bands in the range 3600–2900 cm^{-1} and relative intensities (%) of zoisite IR-bands 2, 4, and 5 (all at 25 °C)

Sample	Zo 3	Zo 1	Zo 2	Zo 4	Zo 5
Zoisite (X_{ps})	0.0 (0)	0.035 (12)	0.062 (23)	0.096 (23)	0.116 (19)
Relative bulk intensities					
Zo	100	100	100	71	38
Czo	0	0	0	29	62
Relative intensities of zoisite bands					
2	11	9	10	14	17
4	0	6	8	10	16
5	89	85	82	76	67

Note: X_{ps} = Fe^{3+} / (Fe^{3+} + Al – 2); clinozoisite composition unknown (see text); errors in parantheses represent 2σ.

relative intensity of band 2 shows no clear correlation to iron content (Table 8).

In the spectral range 2250 to 2000 cm^{-1} zoisite displays a pronounced band at ~2170 cm^{-1} (band 9; Fig. 8b) with satellites at ~2195 and ~2140 cm^{-1} (bands 8 and 10) (Table 7). No clinozoisite bands are present in this spectral range.

The positions of the main zoisite bands 2, 4, 5, and 9 change with increasing iron content (Table 7, Fig. 9). Band 2 significantly shifts to lower wavenumbers with an offset between

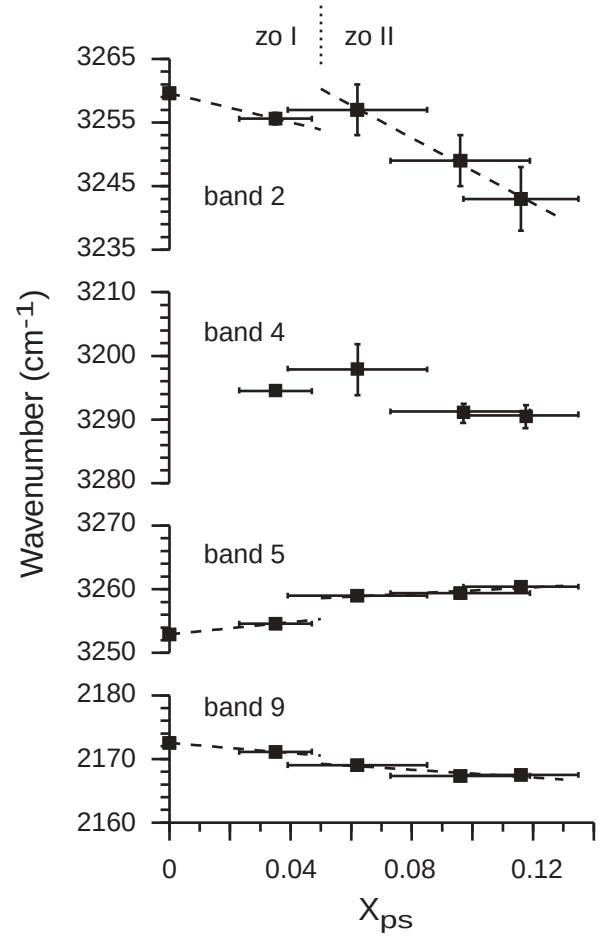

FIGURE 9. Positional shifts of zoisite IR bands 2, 4, 5, and 9 with increasing iron content. Bands 2 and 9 correlate negatively whereas band 5 correlates positively with iron content. Band 4, which is absent in Fe-free zoisite I, shows no clear correlation.

zoisite I and II, whereas band 5 shifts to higher wavenumbers. Band 4 shows no clear correlation between position and iron content. Like band 2, band 9 shifts to lower wavenumbers with increasing iron content, although this shift is only moderate (Fig. 9).

With decreasing temperature bands 2, 4, and 5 of zoisite from sample Zo 5 shift linearly to lower wavenumbers, whereas band 9 shifts to higher ones (Table 9, Fig. 10). Regression lines show that the temperature dependency of bands 4 and 5 is nearly identical (Fig. 10).

DISCUSSION

X-ray diffraction and zoisite modifications I and II

Because the refined lattice constants reflect peak positions whereas the refined fractional atom coordinates are derived from peak intensities, the convergence of the results of these two independent variables strongly suggest that sharp structural discontinuities must occur at ~0.05 X_{ps} in synthetic zoisite. Other possible explanations, such as order-disorder phenom-

TABLE 9. Positions (cm^{-1}) and widths (full width at half maximum FWHM) (cm^{-1}) of selected zoisite IR bands from run Zo 5 [zoisite composition: X_{ps} = 0.116 (19)] at –180 °C, –80 °C, 25 °C, and 125 °C

Temperature	–180 °C	–80 °C	25 °C	125 °C
		Band 2		
position	3215 (3)	3231 (3)	3243 (5)	3257 (10)
FWHM	68 (18)	62 (10)	52 (23)	62 (32)
		Band 4		
position	3152 (3)	3179 (8)	3190.8 (1.8)	3212 (9)
FWHM	53 (18)	61 (16)	53 (9)	52 (27)
		Band 6		
position	3120.7 (1.7)	3139 (2)	3160.4 (4)	3181.9 (1.4)
FWHM	48 (9)	68 (5)	56.2 (7)	58.9 (1.1)
		Band 9		
position	n.d.	2182.7 (2)	2167.50 (5)	2154.73 (5)
FWHM		27.6 (3)	31.6 (1)	36.92 (15)

Notes: X_{ps} = Fe^{3+} / (Fe^{3+} + Al – 2); n.d. = not determined; errors in parentheses represent 2σ.

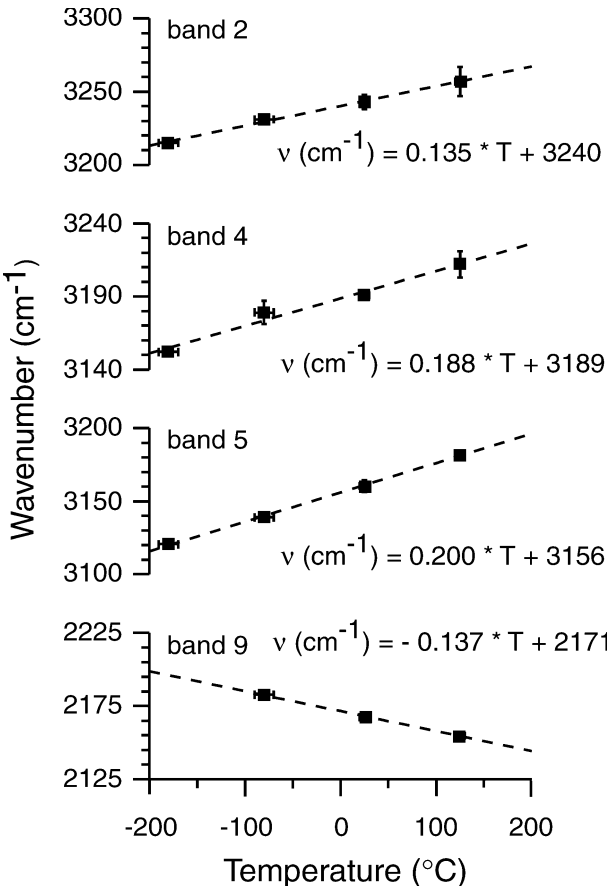

FIGURE 10. Positional shifts of zoisite IR bands 2, 4, 5, and 9 with increasing temperature (samples Zo 5). Bands 2, 4, and 5 correlate positively with temperature, band 9 negatively. The temperature dependency of the position of bands 4 and 5 is slightly larger than that of band 2.

ena, can be ruled out. Ordering of Fe^{3+} and Al between M1,2 and M3 would result in kinks and not in offsets of the refined values. Additionally, the X-ray results give no indication of Fe^{3+} at M1,2. Stacking faults in [100] that would produce monoclinic (clinozoisite) domains (Ray et al. 1986) should result in offsets opposite to those observed, because *a* is shorter in clinozoisite than in zoisite whereas *b* and *c* are longer in clinozoisite. Lastly, effects of preparation are unlikely, because a second series of preparations made for each experiment yielded identical results. Therefore, our data point to two structurally slightly different zoisite modifications.

In natural zoisite, two different optical orientations are known (Myer 1966; Maaskant 1985); in iron-poor β-zoisite the optic axial plane is parallel to (010) and in the iron-rich α-zoisite or ferrian zoisite the optic axial plane is parallel to (100). However, it is an open question whether the transition from β- to α-zoisite with increasing Fe-content is continuous, as postulated by Myer (1966) and Maaskant (1985), or discontinuous. Myer (1966) and Maaskant (1985) postulated that the transformation from β- to α-zoisite occurs at iron contents of ~0.07–0.09 X_{ps}, in fairly good agreement with the present results. Therefore, zoisite I and II might be correlated with β- and α-zoisite, respectively. Unfortunately, we were not able to determine the orientation of the optic axial plane of zoisite in our synthetic samples. Due to the small thickness of the crystals (<<5 μm) the universal stage measurements did not yield unequivocal results. The correlation of zoisite I and II with β- and α-zoisite is therefore only speculative.

The refined lattice constants of this study show differences with respect to published lattice constants of zoisite (Fig. 11). The lattice constants *a*, *b*, and *V* of synthetic iron free zoisites from Langer and Lattard (1980) and Grevel et al. (2000) agree well with the results of this study, whereas the *c* dimensions of Langer and Lattard (1980) and Grevel et al. (2000) are significantly larger. Lattice constants from natural iron bearing zoi-

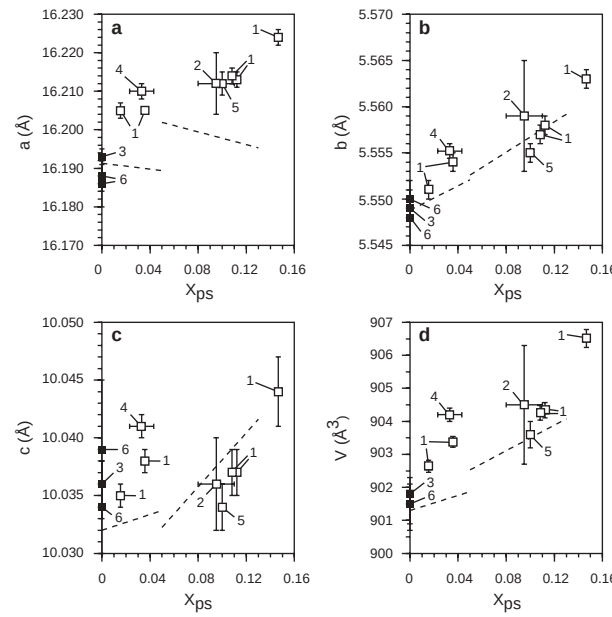

FIGURE 11. Comparison of lattice parameters of synthetic zoisite I and II (dashed lines) with published values for synthetic iron free zoisites (3 = Langer and Lattard 1980; 6 = Grevel et al. 2000) and natural iron bearing zoisites (1 = Myer 1966; 2 = Dollase 1968; 4 = Pawley et al. 1996; 5 = Comodi and Zanazzi 1997).

sites (Myer 1966; Dollase 1968; Pawley et al. 1996; Comodi and Zanazzi 1997) deviate significantly from the results of this study (Fig. 11). Reasons for these differences might be additional minor elements such as Mn^{2+}, Mn^{3+}, V^{3+}, Sr, or REE in the natural samples, and different synthesis conditions.

Fe^{3+}-Al exchange in zoisite. Both zoisite modifications exhibit identical structural responses to increasing iron content, although the structural variations are more pronounced in zoisite II than in zoisite I. Neither zoisite I nor zoisite II show any signs of iron incorporation at the M2 site, in good accordance with Ghose and Tsang (1971) and contrary to clinozoisite in which iron partitions between the three M1, M2, and M3 octahedra of the monoclinic structure as a function of *T* and total iron content (Giuli et al. 1999). In zoisite I and II the M3 octahedron expands significantly in the **a** direction and flattens moderately in **b** with increasing iron content (Fig 12a). The expansion in **a** results in displacement of the apical O8 atom (Fig. 12a, b), which is compensated for by rotation of the T2 tetrahedron around the relatively fixed apical O3 atom of the M1,2 octahedron (Fig. 12b). The rotation of T2 leads to rotation of the corner-linked T1 tetrahedron in the opposite direction (Fig. 12b), which is reflected by the increasing O8-O9-O7 angle of the Si_2O_7 group. The tilting of T1 and T2 expands the Si_2O_7 group in the **c** direction and is responsible for the observed inflation of the structure parallel to **c**.

This response of the zoisite structure to increasing iron content in M3 might explain the existence of zoisite I and II. Increasing rotation of T1 and T2 increases the strain of the zoisite structure that, in turn, most probably limits the degree of rotation of T1 and T2. In the case of zoisite I the stress caused by rotation of T1 and T2 is released by expansion of the structure parallel to **a**, a back-rotation of T1 and T2 into their normal positions and consequently by the formation of zoisite II. Zoisite II is able to compensate for further iron incorporation by rotation of T1 and T2. We speculate that, at a critical iron content, zoisite II breaks down to form monoclinic clinozoisite.

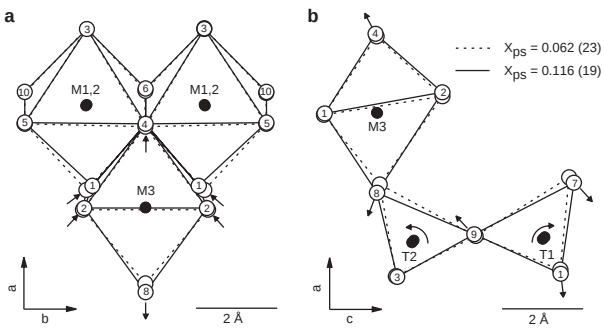

FIGURE 12. Structural variation of zoisite II with increasing iron content. With increasing iron content M3 elongates significantly in **a** and flattens slightly in **b** (**a**). The expansion of M3 parallel to **a** is compensated by a rotation of T2 around the relatively fixed apical O3 atom of the parallel octahedral chain (**b**). This rotation results in an opposite rotation of T1, enlarging the structure parallel to **c**. Due to the opposite rotation of T1 and T2, both the O7-O9-O8 angle and the O7-O8 distance increase (**b**).

***P-V-T* behavior of zoisite.** The two zoisite modifications might explain the different results of previous studies on the *P-V-T* behavior of zoisite. Comodi and Zanazzi (1997) determined a bulk modulus of $K_{298}^{zo} = 114$ GPa for a natural zoisite with ~0.10 X_{ps} whereas Pawley et al. (1998) found $K_{298}^{zo} = 125$ GPa for a natural zoisite with 0.023–0.043 X_{ps}. The latter bulk modulus is identical to that of a synthetic iron-free zoisite (Grevel et al. 2000). Comodi and Zanazzi (1997) and Pawley et al. (1998) postulate for the compression mechanism not only a shrinkage of individual polyhedra but also a rotation of polyhedra and especially of the T1 and T2 tetrahedra. The composition of the zoisite studied by Comodi and Zanazzi (1997) corresponds to zoisite II of this study whereas the compositions of the zoisites studied by Pawley et al. (1998) and Grevel et al. (2000) correspond to zoisite I. Therefore the different bulk moduli might reflect the structural differences between zoisite I and II. In particular, rotation of T1 and T2 as a response to pressure-induced compression is probably easier in zoisite II than in zoisite I, which would explain the lower bulk modulus of zoisite II.

Using $(\partial V/\partial X)$ for this study for zoisite I and zoisite II, a $K_{298}^{zo\,I}$ of 125 GPa (Pawley et al. 1998; Grevel et al. 2000) and a $K_{298}^{zo\,II}$ of 114 GPa (Comodi and Zanazzi 1997), and the isobaric thermic extensional coefficient of Pawley et al. (1996) of $a_0 = 3.86 \times 10^{-5}$ K^{-1} for zoisite I and II, the complete *P-V-T-X* expressions for zoisite I and II are:

$$V^{zo\,I}\,[cm^3/mol] = V_0^{zo\,I} \times (1 + 1.26 \times 10^{-2} \times X_{ps}) \times (1 + \alpha_0^{zo} \times T') \times (1 - \beta_V^{zo\,I} \times P)$$

$$V^{zo\,II}\,[cm^3/mol] = V_0^{zo\,II} \times (1 + 2.14 \times 10^{-2} \times X_{ps}) \times (1 + \alpha_0^{zo} \times T') \times (1 - \beta_V^{zo\,II} \times P),$$

with $V_0^{zo\,I} = 135.69$ cm^3/mol, $V_0^{zo\,II} = 135.74$ cm^3/mol, $\alpha_0^{zo} = 3.86 \times 10^{-5}$ K^{-1}, $\beta_V^{zo\,I} = 8.00 \times 10^{-3}$ GPa^{-1}, $\beta_V^{zo\,II} = 8.77 \times 10^{-3}$ GPa^{-1}, $T' = (T–298)$ K and *P* in GPa.

Taking $K_{298}^{czo} = 130$ GPa (Comodi and Zanazzi 1997), $\alpha_0^{czo} = 2.94 \times 10^{-5}$ K^{-1} (Pawley et al. 1996), and $(\partial V/\partial X)$ for clinozoisite fitted to published cell volumes (Seki 1959; Myer 1966; Dollase 1968; Gabe et al. 1973; Kvik et al. 1988; Bonazzi and Menchetti 1995; Della Ventura et al. 1996; Pawley et al. 1996), zoisite has a smaller cell volume than clinozoisite with identical composition under geologically reasonable *P-T-X* conditions. Bearing in mind that clinozoisite always has higher iron contents than coexisting zoisite (Enami and Banno 1980; Franz and Selverstone 1992; Brunsmann et al. 2002) zoisite should structurally be the high-pressure modification.

Assignment of IR bands

Spectral range 3600–2900 cm^{-1}. The positional shifts and changes in relative intensities of the zoisite bands 2, 4, and 5, combined with the results from X-ray powder diffraction, allow assignment of these bands to discrete local environments. The positive correlation with temperature (Table 9, Fig. 10) shows that all are due to OH stretching vibrations. According to Ito et al. (1954), Hanisch and Zemann (1966), Dollase (1968), Linke (1970), Gabe et al. (1973), and Smith et al. (1987), the proton in zoisite is bonded to the O10 atom to form a hydrogen bridge to O4 of the parallel octahedral chain. The O10 atom is

linked to two adjacent M1,2 octahedra, but the O4 atom is linked to two adjacent M1,2 octahedra and one M3 octahedron. Because M3 either houses Al or Fe^{3+}, two different local environments of the OH-group can be distinguished, one with Al at M3 and one with Fe^{3+} at M3. Consequently, and following Langer and Raith (1974), the most significant band (5) is assigned to the stretching vibration of the configuration

$$Al^{[M1,2]}Al^{[M1,2]}–O10–H\cdots O4–Al^{[M1,2]}Al^{[M1,2]}Al^{[M3]}.$$

Band 4, which is only present in iron bearing zoisite and the intensity of which increases with increasing iron content, must be assigned to the stretching vibration of the configuration

$$Al^{[M1,2]}Al^{[M1,2]}–O10–H\cdots O4–Al^{[M1,2]}Al^{[M1,2]}Fe^{3+[M3]}.$$

The slightly higher energy of band 4 compared to band 5 is related to the distortion of M3 caused by the iron incorporation, which slightly increases the distance between O10 and O4. According to Langer and Raith (1974), bands 3 and 7 and 1 and 6, respectively, are interpreted as combinations of bands 4 and 5 with lattice vibrations at ~100 cm^{-1}. Because for Al,Fe^{3+}-zoisite only the two configurations described above for O10–H···O4 are possible, band 2 must arise from a second hydrogen bridge (Ox–H···Oy). Total bond strengths of anions, calculated for the refined zoisite structures with the data of Brese and O'Keeffe (1991) show that beside O10, which is strongly undersaturated, only O1, O2, and O8 are possible candidates for Ox and Oy (Table 10). From the position of band 2 the length of the underlying hydrogen bridge Ox–H···Oy can be calculated (Bellamy and Owens 1969). The results show that it decreases from ~2.718 to ~2.710 Å with increasing iron content, displaying an offset between zoisite I and zoisite II (Fig. 13a). Calculation of all possible O-O distances for O1, O2, and O8 from the XRD data shows that only O10-O2 displays a comparable correlation with iron content, although the absolute values calculated with the XRD data are larger than those calculated from the IR data (Fig. 13b). We therefore assign band 2 to the configuration

$$Al^{[M1,2]}Al^{[M1,2]}–O10\text{-}H\cdots O2–(Al,Fe^{3+})^{[M3]}.$$

Such a second hydrogen bridge O10–H···O2 was previously discussed, but not proven, by Smith et al. (1987). Because the O10 atom and the proton are lying on a mirror plane whereas O2 is at a general position, this hydrogen bridge should be bifurcated. The O10 atom and the proton are always at the same distance from two symmetrically arranged O2 atoms and the charge distribution between the O2 and O10 atoms and the proton must also be symmetrical. A bifurcation is consistent with the erroneously shorter lengths of the hydrogen bridge calculated with the IR vs. the XRD data (Nakamoto et al. 1955; Libowitzky 1999). Based on these assumptions, O10–H···O2 in Fe-zoisite should split into two distinct bands, one for Al at M3 and one for Fe^{3+} at M3. This splitting is, however, not resolvable in most iron-rich samples due to the low intensity of band 2 and to the superimposed clinozoisite IR bands.

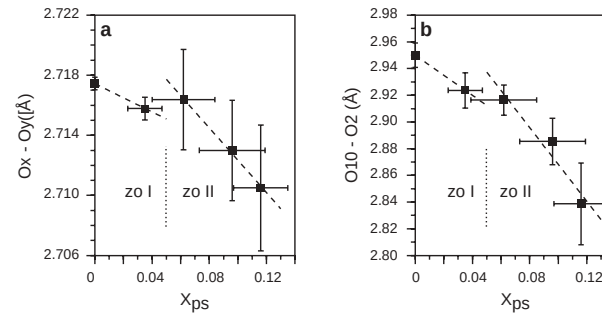

FIGURE 13. Calculated O-O distances for the proposed second hydrogen bridge that is responsible for IR band 2 in zoisite. Calculations are based on IR (**a**) and XRD data (**b**). In both cases there is a good inverse correlation with iron content, with a slight positive offset between zoisite I and II. The distances calculated with the XRD data are somewhat larger, which is explained by the bifurcated underlying hydrogen bridge (see text for explanation).

TABLE 10. Total bond strengths of anions in synthetic zoisites

Sample	Zo 3	Zo 1	Zo 2	Zo 4	Zo 5
Zoisite (X_{Fe})	0.0 (0)	0.035 (12)	0.062 (23)	0.096 (23)	0.116 (19)
O1	1.84 (9)	1.79 (9)	1.81 (9)	1.72 (14)	1.7 (2)
O2	1.78 (9)	1.81 (9)	1.78 (9)	1.77 (14)	1.8 (3)
O4	1.79 (9)	1.73 (9)	1.77 (9)	1.74 (14)	1.7 (2)
O7	1.92 (10)	1.94 (10)	2.00 (10)	1.85 (15)	1.9 (3)
O8	1.77 (9)	1.81 (9)	1.84 (9)	1.84 (15)	2.0 (3)
O3	2.16 (11)	2.13 (11)	2.13 (11)	2.12 (17)	2.0 (3)
O5	2.19 (11)	2.16 (11)	2.18 (11)	2.12 (17)	2.1 (3)
O6	2.04 (10)	2.10 (10)	2.05 (10)	2.16 (17)	2.1 (3)
O9	1.98 (10)	2.10 (10)	2.05 (10)	2.16 (17)	2.4 (3)
O10 *	1.17 (6)	1.10 (6)	1.15 (6)	1.14 (9)	1.02 (14)

Note: $X_{ps} = Fe^{3+}/(Fe^{3+} + Al - 2)$; errors in parentheses represent 2σ* without H.

The band 9 at ~2170 cm^{-1}. The negative correlation of band 9 with temperature indicates that this band cannot be due to a stretching vibration, as proposed by Langer and Raith (1974), but is typical for bending vibrations (Novak 1974; Hadzi and Bratos 1976). Winkler et al. (1989) interpreted band 9 as the first overtone of the "in-plane" bending vibration of the O10–H···O4 hydrogen bridge. The question arises as to why such a band is not found in clinozoisite, although the environment of the O10–H···O4 hydrogen bridge in clinozoisite is comparable to that in zoisite (Langer and Raith 1974). Additionally, the first overtone of the bending vibration of a straight hydrogen bridge should be in the range of ~1950–2000 cm^{-1} (Stubican and Roy 1961; Vedder and McDonald 1963; Russel et al. 1970). We therefore interpret band 9 as the first overtone of the "in-plane" bending vibration of the O10–H···O2 hydrogen bridge. The lack of a comparable band in clinozoisite is due to the absence of the underlying hydrogen bridge. The bifurcated nature of O10–H···O2 explains the relatively high energy of band 9. To test our interpretation of both bands 9 and 2, further studies should focus on polarized single-crystal IR spectroscopy.

Zoisite I–zoisite II phase transition

Within precision our data show no change in symmetry and no framework reconstruction between zoisite I and zoisite II.

The transformation from zoisite I to zoisite II is therefore best classified as an isosymmetric displacive phase transition induced by solid solution. An isosymmetric displacive transformation induced by temperature has been reported for malayaite, $CaSnSiO_5$, (Bismayer et al. 1999), a rare mineral isostructural with titanite and found in skarn deposits (Higgins and Ribbe 1977). The latter transformation is characterized by a tumbling motion of the SnO_6 octahedra (Bismayer et al. 1999; Zhang et al. 1999).

The principal mechanism by which the zoisite I and II structures response to the stress caused by the substitution of the larger Fe^{3+} ion for Al is identical to that reported for the expansion of the zoisite structure as a function of *T* and *P* (Comodi and Zanazzi 1997; Pawley et al. 1998; Grevel et al. 2000). Relative individual deformations as a function of iron content in zoisite I and II vary in the order $b/b_0 > c/c_0 >> a/a_0$, with $a/a_0 < 0$ (subscript 0 denotes the lattice constants of iron-free zoisite I and II, respectively), individual expansivities and compressibilities in the order $c > b >> a$ (Pawley et al. 1998). The analogy between substitutional- and temperature-induced deformation is also highlighted by the fact that *a* gets shorter both with increasing iron content and with increasing temperature (Pawley et al. 1996). Such an analogy between the effects of temperature and composition is also found in leucite. Palmer et al. (1997) showed that the substitution of the larger Cs or Rb atom for K in leucite produces the same style of framework distortion as that associated with increasing temperature.

Because of the similar effects of composition, temperatures, and pressure on distortion of the zoisite structure, the zoisite I–zoisite II transition should not only depend on composition but also on *P* and *T* (Heaney 2000). This would be in analogy to the leucite system in which a phase transition occurs that can either be induced by temperature or by solid solution, although the transition in the leucite system is not isosymmetric but includes a change from cubic (high-*T* form) to tetragonal (low-*T* form) symmetry (Martin and Lagache 1975; Palmer et al. 1997). The transition temperature in leucite decreases with increasing size of the substituted cation and with increasing Cs or Rb content (Palmer et al. 1997). Combining the data from the leucite system with our results, (1) the zoisite I–zoisite II transition should not only be induced by solid solution but also by *P* and *T*, (2) zoisite II should be the high-temperature, low-pressure modification, and (3) the transition temperature from zoisite I to zoisite II should be negatively correlated with the iron content.

A reevaluation of the published *P-V-T* data for zoisite (Holland et al. 1996; Pawley et al. 1996; Comodi and Zanazzi 1997; Pawley et al. 1998; Grevel et al. 2000) in the light of our new results, unfortunately did not show any clear discontinuities in lattice parameters due to varying *P* or *T* that would point to the zoisite I–zoisite II phase transition. This can either be due to the small differences between zoisite I and II that might be masked by the analytical uncertainties, or to the fact that the *P-T* conditions of the phase transition simply lie outside the studied *P-T* ranges. We therefore emphasize that future studies on zoisite should focus on the determination of the *P-T-X* conditions of the zoisite I–zoisite II phase transition. This knowledge will help to constrain the stability fields of zoisite I and II and the phase relations between zoisite and minerals like clinozoisite, lawsonite, and grandite.

ACKNOWLEDGMENTS

The help of I. Bauer from GFZ-Potsdam with the XRD and FTIR measurements and of U. Gernert from TU-Berlin with the REM studies is gratefully acknowledged. The paper benefited from helpful discussions with W. Heinrich and careful reading by D. Lattard. This work was funded by grant Fr 557/11-1,2 of the Deutsche Forschungs Gesellschaft (DFG) and is part of A.L.'s Ph.D. thesis.

REFERENCES CITED

Bellamy, L.J. and Owens, A.J. (1969) A simple relationship between the infrared stretching frequencies and the hydrogen bond distance in crystals. Spectrochimica Acta, 25A, 329–333.

Bismayer, U., Zhang, M., Groat, L.A., Salje, E.K.H, and Meyer, H.-W. (1999) The β-γ phase transition in titanite and the isosymmetric analogue in malayaite. Phase Transitions, 68, 545–556.

Bonazzi, P. and Menchetti, S. (1995) Monoclinic members of the epidote group: effects of the $Al \leftrightarrow Fe^{3+} \leftrightarrow Fe^{2+}$ substitution and of the entry of REE^{3+}. Mineralogy and Petrology, 53, 133–153.

Brese, N.E. and O'Keeffe, M. (1991) Bond-valence parameters for solids. Acta Crystallographica, B 47, 192–197.

Brunsmann, A., Franz, G., Erzinger, J., and Landwehr, D. (2000) Zoisite- and clinozoisite-segregations in metabasites (Tauern Window, Austria) as evidence for high-pressure fluid-rock interaction. Journal of Metamorphic Geology, 18, 1–21.

Brunsmann, A., Franz, G., and Heinrich, W. (2002) Experimental investigation of zoisite-clinozoisite phase equilibria in the system $CaO-Fe_2O_3-Al_2O_3-SiO_2-H_2O$. Contributions to Mineralogy and Petrology, 143,115–130.

Caglioti, G., Paoletti, A., and Ricci, F.P. (1958) Choice of collimators for crystal spectrometer for neutron diffraction. Nuclear Instruments, 3, 223–228.

Comodi, P. and Zanazzi, P.F. (1997) The pressure behavior of clinozoisite and zoisite: An X-ray diffraction study. American Mineralogist, 82, 61–68.

Della Ventura, G., Mottana, A., Parodi, G.C., and Griffin, W.L. (1996) FTIR spectroscopy in the OH-stretching region of monoclinic epidotes from Praborna (St. Marcel, Aosta valley, Italy). European Journal of Mineralogy, 8, 655–665.

Dollase, W.A. (1968) Refinement and comparison of the structures of zoisite and clinozoisite. American Mineralogist, 53, 1882–1898.

Enami, M. and Banno, S. (1980) Zoisite-clinozoisite relations in low- to medium-grade high-pressure metamorphic rocks and their implications. Mineralogical Magazine, 43, 1005–1013.

Fesenko, E.G., Rumanova, I.M., and Belov, N.V. (1955) The crystal structure of zoisite. Structure Reports, 19, 464–465.

———(1956) Crystal structure of zoisite. Structure Reports, 20, 396–398.

Franz, G. and Selverstone, J. (1992) An empirical phase diagram for the clinozoisite-zoisite transformation in the system $Ca_2Al_3Si_3O_{12}(OH)$-$Ca_2Al_2Fe^{3+}Si_3O_{12}(OH)$. American Mineralogist, 77, 631–642.

Gabe, E.J., Portheine, F.C., and Whitlow, S.H. (1973) A reinvestigation of the epidote structure: confirmation of the iron location. American Mineralogist, 58, 218-223.

Ghose, S. and Tsang, T. (1971) Ordering of V^{2+}, Mn^{2+}, and Fe^{3+} ions in zoisite, $Ca_2Al_3Si_3O_{12}(OH)$. Science, 171, 374–376.

Giuli, G., Bonazzi, P., and Menchetti, S. (1999) Al-Fe disorder in synthetic epidotes: A single-crystal X-ray diffraction study. American Mineralogist, 84, 933–936.

Gottschalk, M. (1994) How to synthesize large amphiboles: method and first results. 16th IMA General Meeting, Pisa/Italy, abstract vol., 153.

Grevel, K.-D., Nowlan, E.U., Fasshauer, D.W., and Burchard, M. (2000) In situ X-ray diffraction investigation of lawsonite and zoisite at high pressures and temperatures. American Mineralogist, 85, 206–216.

Griffiths, P.R. and de Haseth, J.A. (1986) Fourier transform infrared spectroscopy. Chemical Analysis, 83, Wiley, New York.

Hadzi, D. and Bratos, S. (1976) Vibrational spectroscopy of the hydrogen bond. In P. Schuster, G. Zundel, and C. Sandorfy, Eds., The hydrogen bond. Vol II. North Holland Publishing Company, Amsterdam.

Hanisch, K. and Zemann, J. (1966) Messung des Ultrarot-Pleochroismus von Mineralen. IV. Der Pleochroismus der OH-Streckfrequenz in Epidot. Neues Jahrbuch für Mineralogie, Monatshefte, 19–23.

Heaney, P.J. (2000) Phase transformations induced by solid solution. In S.A.T. Redfern and M.A. Carpenter, Eds., Transformation Processes in Minerals. Reviews in Mineralogy and Geochemistry, 39, 135–174.

Higgins, J.B. and Ribbe, P.H. (1977) The structure of malayaite, $CaSnSiO_5$, a tin analog of titanite. American Mineralogist, 62, 801–806.

Holland, T.J.B., Redfern, S.A.T., and Pawley, A.R. (1996) Volume behavior of hydrous minerals at high pressure and temperature: II. Compressibilities of lawsonite, zoisite, clinozoisite, and epidote. American Mineralogist, 81, 341–348.

Ito, T., Morimoto, N., and Sadanga, R. (1954) On the structure of epidote. Acta

Crystallographica, 7, 53–59.
Kvik, Å., Pluth, J.J., Richardson Jr., J.W., and Smith, J.V. (1988) The ferric iron distribution and hydrogen bonding in epidote: a neutron diffraction study at 15 K. Acta Crystallographica, B 44, 351–355.
Langer, K. and Lattard, L. (1980) Identification of a low-energy OH-valence vibration in zoisite. American Mineralogist, 65, 779–783.
Langer, K. and Raith, M. (1974) Infrared spectra of Al-Fe(III)-epidotes and zoisites, $Ca_2(Al_{1-p}Fe^{3+}_p)Al_2O(OH)[Si_2O_7][SiO_4]$. American Mineralogist, 59, 1249–1258.
Larson, A.C. and Von Drele, R.B. (1987) Generalized structure analysis system. Los Alamos National Laboratory Report No. LA-UR-86-748.
Libowitzky, E. (1999) Correlation of O-H stretching frequencies and O-H ... H hydrogen bond lengths in minerals. Monatshefte für Chemie, 130, 1047-1059.
Linke, W. (1970) Messung des Ultrarot-Pleochroismus von Mineralen. X. Der Pleochroismus der OH-Streckfrequenz in Zoisit. Tschermaks Mineralogische und Petrographische Mitteilungen, 14, 61–63.
Maaskant, P. (1985) The iron content and the optic axial angle in zoisites from Galicia, NW Spain. Mineralogical Magazine, 49, 97–100.
Martin, R.F. and Lagache, M. (1975) Cell edges and infrared spectra of synthetic leucites and pollucites in the system $KAlSi_2O_6$-$RbAlSi_2O_6$-$CsAlSi_2O_6$. Canadian Mineralogist, 13, 275–281.
Merz, L. (1965) Transformation in Optics. Wiley, New York.
Myer, G.H. (1966) New data on zoisite and epidote. American Journal of Science, 264, 364–385.
Nagasaki, A. and Enami, M. (1998) Sr-bearing zoisite and epidote in ultra-high pressure (UHP) metamorphic rocks from the Su-Lu province, eastern China: an important Sr reservoir under UHP conditions. American Mineralogist, 83, 240–247.
Nakamoto, K., Margoshes, M., and Rundle, R.E. (1955) Stretching frequencies as a function of distances in hydrogen bonds. Journal of the American Chemical Society, 77, 6480–6486.
Novak, A. (1974) Hydrogen bonding in solids: Correlation of spectroscopic and crystallographic data. Structure and Bonding, 82, 85–103.
Palmer, D.C., Dove, M.T., Ibberson, R.M., and Powell, B.M. (1997) Structural behavior, crystal chemistry, and phase transitions in substituted leucite: High-resolution neutron powder diffraction studies. American Mineralogist, 82, 16–29.
Pawley, A.R., Redfern, S.A.T., and Holland, T.J.B. (1996) Volume behavior of hydrous minerals at high pressure and temperature: I. Thermal expansion of lawsonite, zoisite, clinozoisite, and diaspore. American Mineralogist, 81, 335–340.
Pawley, A.R., Chinnery, N.J., and Clark, S.M. (1998) Volume measurements of zoisite at simultaneously elevated pressure and temperature. American Mineralogist, 83, 1030–1036.
Poli, S. and Schmidt, M.W. (1998) The high-pressure stability of zoisite and phase relationships of zoisite-bearing assemblages. Contributions to Mineralogy and Petrology, 130, 162–175.
Pouchou, J.L. and Pichoir, F. (1984) Un nouveau modèle de calcul pour la microanalyse quantitative par spectrométrie de rayons X. La Recherche Aérospatiale, 3, 167–192.
Ray, N.J., Putnis, A., and Gillet, P. (1986) Polytypic relationship between clinozoisite and zoisite. Bulletin Mineralogie, 109, 667–685.
Russel, J.D., Farmer, V.C., and Velde, B. (1970) Replacement of OH by OD in layer silicates, and identification of the vibrations of these groups in infra-red spectra. Mineralogical Magazine, 77, 292, 869–879.
Schmidt, M.W. and Poli, S. (1994) The stability of lawsonite and zoisite at high pressures: Experiments in CASH to 92 kbar and implications for the presence of hydrous phases in subducted lithosphere. Earth and Planetary Science Letters, 124, 105–118.
Seki, Y. (1959) Relation between chemical composition and lattice constants of epidote. American Mineralogist, 44, 720–730.
Smith, J.V., Pluth, J.J., Richardson Jr., J.W., and Kvick, Å. (1987) Neutron diffraction study of zoisite at 15 K and X-ray study at room temperature. Zeitschrift für Kristallographie, 179, 305–321.
Stubican, V. and Roy, R. (1961) Isomorphous substitution and infrared spectra of the layer lattice silicates. American Mineralogist, 46, 32–51.
Tröger, W.E. (1982) Optische Bestimmung der gesteinsbildenden Minerale. Teil 1. Bestimmungstabellen, 188 p. E. Schweizerbartśche Verlagsbuchhandlung, Stuttgart.
Vedder, W. and McDonald, R.S. (1963) Vibrations of OH-ions in muscovite. Journal of Chemistry and Physics, 38, 1583–1590.
Winkler, B., Langer, K., and Johannsen, P.G. (1989) The influence of pressure on the OH valence vibration of zoisite. Physics and Chemistry of Minerals, 16, 668–671.
Zhang, M., Meyer, H.-W., Groat, L.A., Bismayer, U., Salje, E.K.H., and Adiwidjaja, G. (1999) An infrared spectroscopic and single-crystal X-ray study of malayaite, $CaSnSiO_5$. Physics and Chemistry of Minerals, 26, 546–553.
Zimmermann, R., Heinrich, W., and Franz, G. (1996) Tremolite synthesis from $CaCl_2$-bearing aqueous solutions. European Journal of Mineralogy, 8, 767–776.

MANUSCRIPT RECEIVED MARCH 28, 2001
MANUSCRIPT ACCEPTED FEBRUARY 4, 2002
MANUSCRIPT HANDLED BY JEFFREY E. POST